

“This document is the Accepted Manuscript version of a Published Work that appeared in final form in *Nano Letters*, copyright © American Chemical Society after peer review and technical editing by the publisher. To access the final edited and published work see:

<https://dx.doi.org/10.1021/acs.nanolett.5b05125>”

Twin-induced InSb nanosails: a convenient high mobility quantum system

María de la Mata,^{1,‡} Renaud Leturcq,^{2,3,‡} Sébastien R. Plissard,⁴ Chloé Rolland,^{2,‡} César Magén,⁵ Jordi Arbiol,^{1,6,*} and Philippe Caroff,^{2,7,*}*

¹Catalan Institute of Nanoscience and Nanotechnology (ICN2), CSIC and The Barcelona Institute of Science and Technology, Campus UAB, Bellaterra, 08193 Barcelona, Spain

²Institut d'Électronique, de Microélectronique et de Nanotechnologie, UMR CNRS 8520, Avenue Poincaré, C.S. 60069, 59652 Villeneuve d'Ascq, France

³Materials Research and Technology (MRT) Department, Luxembourg Institute of Science and Technology (LIST), 5, avenue des Hauts-Fourneaux, L-4362 Esch-sur-Alzette, Luxembourg

⁴CNRS-Laboratoire d'Analyse et d'Architecture des Systèmes (LAAS), Université de Toulouse, 7 avenue du colonel Roche, 31400 Toulouse, France

⁵Laboratorio de Microscopías Avanzadas (LMA), Instituto de Nanociencia de Aragon (INA) - ARAID, and Departamento de Física de la Materia Condensada, Universidad de Zaragoza, 50018 Zaragoza, Spain

⁶Institució Catalana de Recerca i Estudis Avançats (ICREA), 08010 Barcelona, Catalonia, Spain

1
2
3 ⁷Department of Electronic Materials Engineering, Research School of Physics and Engineering,
4
5
6 The Australian National University, Canberra, ACT 0200, Australia
7
8
9
10
11
12
13

14
15 ABSTRACT
16

17
18
19 Ultra-narrow bandgap III-V semiconductor nanomaterials provide a unique platform for realizing
20
21 advanced nanoelectronics, thermoelectrics, infra-red photodetection and quantum transport
22
23 physics. In this work we employ molecular beam epitaxy to synthesize novel nanosheet-like InSb
24
25 nanostructures exhibiting superior electronic performance. Through careful morphological and
26
27 crystallographic characterization we show how this unique geometry is the result of a single
28
29 twinning event in an otherwise pure zinc blende structure. Four-terminal electrical measurements
30
31 performed in both the Hall and van der Pauw configurations reveal a room temperature electron
32
33 mobility greater than $12,000 \text{ cm}^2 \cdot \text{V}^{-1} \cdot \text{s}^{-1}$. Quantized conductance in a quantum point contact
34
35 processed with a split-gate configuration is also demonstrated. We thus introduce InSb
36
37 ‘nanosails’ as a versatile and convenient platform for realizing new device and physics
38
39 experiments with a strong interplay between electronic and spin degrees of freedom.
40
41
42
43
44
45

46
47 KEYWORDS III-V Semiconductor, Nanowires, Molecular Beam Epitaxy, Hall measurements,
48
49 Quantum Point Contact, Cs-corrected Scanning Transmission Electron Microscopy.
50
51

52
53
54 High-quality narrow bandgap III-V semiconductor nanostructures hold promise for applications
55
56 in infra-red optoelectronics^{1,2}, low-power nanoelectronics^{3,4} and quantum physics⁵. Until now,
57
58
59
60

1
2
3 reports have focused on the nanowire geometry which has been used to demonstrate direct
4
5 integration on silicon⁶, gate-all-around (tunnel) field effect transistors⁷⁻⁹, efficient IR
6
7 photodetection,^{10, 11} lasing¹²⁻¹⁴ and enhanced thermoelectric performance¹⁵⁻²⁰.
8
9

10
11 With the narrowest bandgap among the III-V semiconductors, InSb is characterized by an
12
13 extremely low effective carrier mass and therefore has the potential to realize some of the highest
14
15 values of electron mobility among all semiconductors. Coupled with the largest Landé g-factor
16
17 of all semiconductors,²¹ and the fact that peak electron velocity occurs at relatively low electric
18
19 fields, InSb is an ideal material for high speed and low power nanoelectronics²² and 0D/1D
20
21 electron or hole systems for quantum transport physics²³⁻²⁵. High quality InSb nanowires have
22
23 already been shown to enable fast manipulation of spin-orbit qubits^{24, 26} and have played a key
24
25 role in the search for the elusive Majorana fermion²⁷⁻²⁹.
26
27
28
29
30

31 The epitaxial growth conditions and crystal quality of antimonide nanostructures differ
32
33 significantly from those of all other III-Vs due to both the low vapor pressure of Sb and its action
34
35 as a surfactant³⁰. On one hand, these specificities make growth of InSb free-standing
36
37 nanostructures challenging due to the necessity of providing nanowire ‘stems’ to nucleate them
38
39 away from the substrate³¹, impractically slow growth rates in the axial direction³², and the
40
41 existence of very narrow ‘sweet spot’ in the growth parameter space³³. On the other hand, these
42
43 special growth conditions guarantee a perfect crystal structure independently of the growth
44
45 technique³⁴⁻³⁷ a total absence of tapering for nanowires thanks to a very low nucleation
46
47 probability on their {110} sidewalls and the opportunity to tailor the morphology, to deliver
48
49 geometries such as diamond-shaped free-standing 3D nanostructures^{33, 38}, or nanocrosses^{39, 40}.
50
51 While antimonide nanocrystals usually lack planar defects perpendicular to the growth direction,
52
53 the appearance of crystallographic defects in other directions can induce changes in the geometry
54
55
56
57
58
59
60

1
2
3 of the overall system rather than promoting a crystal phase transition, explaining the formation of
4 tilted nanowires⁴¹, branched nanostructures⁴² or kinking phenomena⁴³. Despite these
5
6 achievements, the nanowire geometry has proven impractical for the realization of multi-terminal
7
8 devices such as Hall bars^{44,45}, quantum point contacts or Aharonov-Bohm rings⁴⁶. Realizing
9
10 nanosheets of this material while keeping the advantages already demonstrated by nanowires
11
12 would thus open the way to more advanced device geometries⁴⁷, still enable advanced
13
14 heterostructures⁴⁸, while also significantly easing the device fabrication process⁴⁹. There are
15
16 currently however few reports of free-standing III-V nano-sheets and the majority of these
17
18 examples contain at least a few stacking defects perpendicular to their vertical growth axis⁵⁰⁻⁵⁴.
19
20
21
22
23
24

25
26 Here we show that InSb nanosheets in the form of a vertical nanosail can be grown epitaxially
27
28 from an InAs ‘mast’ acting as a stem, with a thickness controlled by the seed particle, two large
29
30 atomically flat {110} surfaces and a highly faceted geometry. Growth is possible using the two
31
32 main epitaxy techniques, i.e. metalorganic vapour phase epitaxy (MOVPE) and molecular beam
33
34 epitaxy (MBE), but only the latter is detailed here. The nanosail crystal structure grown by MBE
35
36 is confirmed to be pure zinc blende with only a single isolated twin boundary event on the lateral
37
38 side. It is found that the single twin drives the crystal to change its geometry and expand to
39
40 create the observed 2D-like morphology. We then proceed with studying its key electronic
41
42 figures of merit such as mobility and carrier concentration using a multi-terminal device
43
44 configuration. A very high mobility above $12\,000\text{ cm}^2\cdot\text{V}^{-1}\cdot\text{s}^{-1}$ is unambiguously determined both
45
46 at low temperature and room temperature. Finally, we demonstrate for the first time quantized
47
48 conductance in a bottom-up InSb nanomembrane in a quantum point contact (QPC)^{55,56}, in the
49
50 absence of an in-plane applied magnetic field⁵⁷.
51
52
53
54
55
56
57
58
59
60

1
2
3 The InAs/InSb nanowire/nanosail heterostructures were grown on InP (111)B *via* a gold-
4 assisted vapor-liquid-solid mechanism in a Riber 32-P gas-source molecular beam epitaxy
5 (MBE) system following a methodology very similar to that reported by Thelander *et al.*³⁷. The
6 structure consists, from bottom to top, of a short InP/InAs stem followed by the InSb segment.
7
8 The general morphology and faceting was evaluated using a Zeiss Ultra 55 SEM while
9 mechanically detached nanostructures were studied by atomic resolution high angle angular
10 dark-field scanning transmission electron microscopy (HAADF-STEM) using a probe corrected
11 FEI Titan 60–300 equipped with a high brightness field emission gun (XFEG) and a CETCOR
12 corrector from CEOS. All the 3D atomic models here presented have been created using the
13 Rhodius software^{58,59}. Back-gated devices were fabricated by transferring the nanosails onto a
14 thermally oxidized highly-doped Si substrate. Low resistive ohmic contacts were then defined by
15 electron beam lithography on ammonium sulphide passivated nanostructures. For the quantum
16 point contact (QPC) device, two ohmic contacts are realized, followed by the deposition of a 10
17 nm HfO₂ conformal gate dielectric layer by atomic layer deposition, and two split gates defined
18 by electronic lithography. Variable temperature magneto-transport experiments were performed
19 in a helium cryostat with a variable temperature insert allowing measurements from 2.1 to 300
20 K, and magnetic field up to 7 T. The Hall and van der Pauw measurements were performed using
21 the lock-in technique. The quantum point contact measurements were performed with a constant
22 d.c. bias voltage. Full growth, characterization and processing details are given in Supporting
23 Information SA.

24
25
26
27
28
29
30
31
32
33
34
35
36
37
38
39
40
41
42
43
44
45
46
47
48
49
50
51
52 Figure 1(a) presents an as-grown InAs/InSb nanowire ensemble containing nanosails
53 structures. Growth here consisted of axial InP/InAs heterostructure stems topped with an InSb
54 segment. Only the bottom InAs stem and InSb sections are visible in this scanning electron
55
56
57
58
59
60

1
2
3 microscopy (SEM) image. It is clear that while some InAs/InSb heterostructures remain in the
4 shape of standard nanowires³⁵ or even diamond-shaped crystallites^{33,38}, a significant proportion
5 of the InSb segments form flat sail-like nanosheets, which we henceforth refer to as ‘nanosails’.
6
7
8 The variation observed here may be related to the stochastic nature of the Au dewetting process
9
10 which produces a distribution of seed diameters and areal densities and the extreme sensitivity of
11
12 free-standing InSb nanostructures to local growth conditions³¹⁻³³. An illustration of this intrinsic
13
14 sensitivity of InSb to local growth conditions is illustrated in Supporting Figure S1. It can
15
16 therefore be inferred that the specific nucleation event leading to this original InSb nanosail
17
18 morphology has a small probability of occurrence under the studied growth conditions. The
19
20 percentage of nanosails to nanowires is measured to be 5.6% (see Supporting Figure S3). The
21
22 ease of obtaining the nanosail geometry is further confirmed in Supporting Figure S2 where the
23
24 same nanostructures are grown by MOVPE (see Supporting Figure S2).
25
26
27
28
29
30
31
32
33
34
35
36
37
38
39
40
41
42
43
44
45
46
47
48
49
50
51
52
53
54
55
56
57
58
59
60

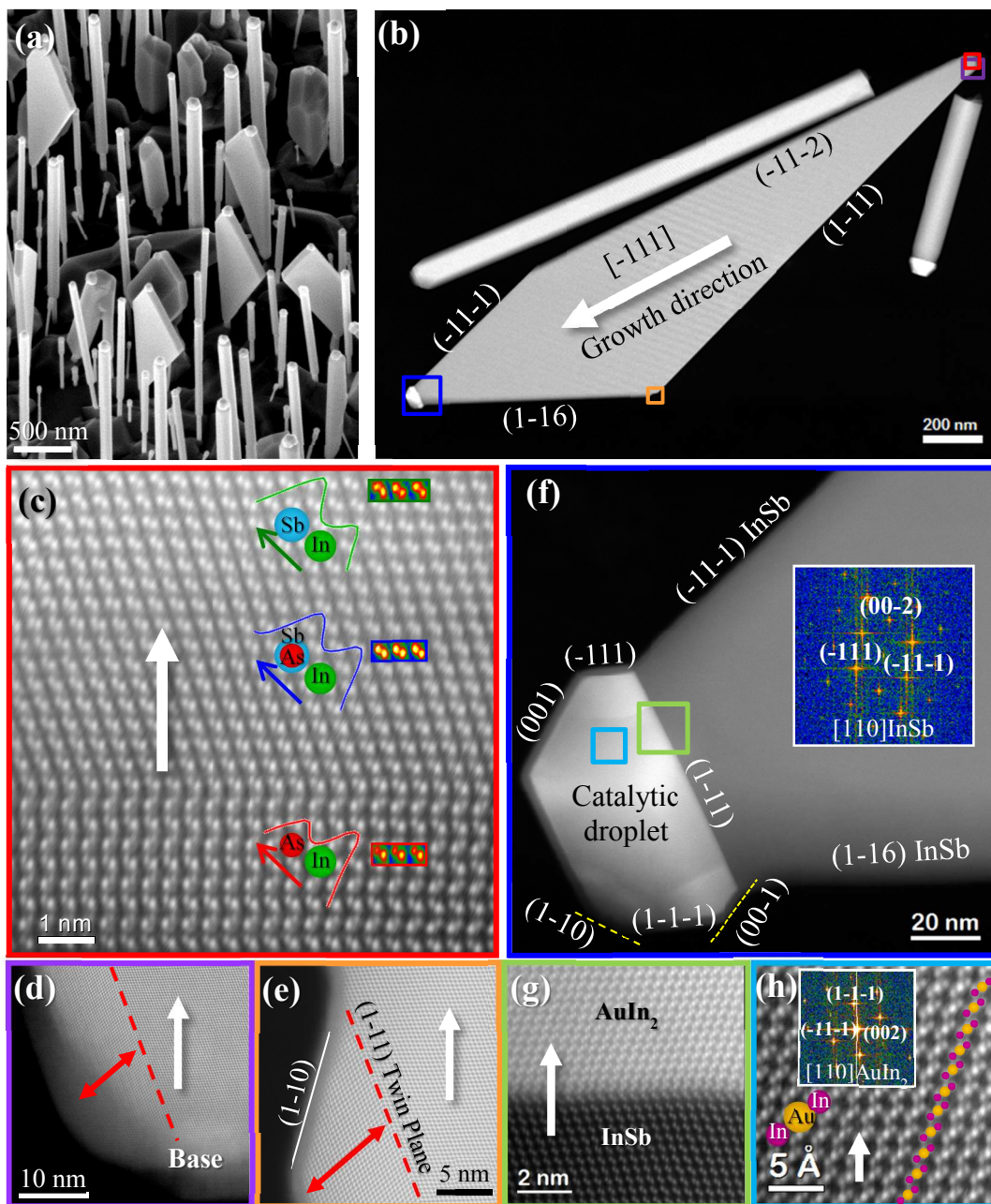


Figure 1. General morphology and crystal structure. (a) SEM image (30° tilt) showing a representative overview of an as-grown InAs/InSb ensemble containing nanosails. (b) Low magnification HAADF image of a nanosail with the regions magnified in c-h indicated by colored squares (c) Atomic resolution HAADF image of the base of the nanosail (growth direction is vertical) showing both WZ InAs and ZB InSb. Red, blue and green curves

1
2
3 correspond to intensity profiles taken along individual dumbbells in order to determine polarity,
4 which was found to be B-polar for both InAs and InSb. (d,e) High resolution images of the twin
5 boundary extending parallel to the $\{111\}$ lateral facet, from the base (d) to its termination (e),
6 where the twinned segment is of constant width (highlighted by the red arrow). (f) Z-contrast
7 image of the nanosail's tip, showing the facets of the AuIn₂ seed particle. A fast Fourier
8 transform (FFT) of the InSb nanosail structure is inset (g) Atomically resolved image of the
9 interphase between the InAs nanosail structure (darker) and the AuIn₂ single crystalline seed
10 particle (brighter) (h) Atomic resolution image of the AuIn₂ structure with FFT inset. Note that
11 the white arrow points indicate the $[\bar{1}11]$ growth direction.
12
13
14
15
16
17
18
19
20
21
22
23
24

25
26 After mechanical dispersion on a holey carbon grid, the nanosails facets were indexed using
27 atomically resolved High Angle Annular Dark Field (HAADF) Scanning Transmission Electron
28 Microscopy (STEM). The primary facets were determined to be $\{110\}$ type bordered by facets of
29 mostly of $\{111\}$ type (Figure 1(b)). Considering the base of the nanosail, Figure 1(c), we observe
30 that the narrow InAs 'mast' segment below the InSb section crystallizes in the wurtzite (WZ)
31 structure while the rest of the sail (composed of pure InSb) presents a pure zinc-blende (ZB)
32 structure (Figure 1(c)). The polarity of the growth direction is further confirmed to be anionic or
33 'B' type by measuring the intensity profile along dumbbells (colored curves in Figure 1(c))⁶⁰.
34 This analysis also reveals the presence of As in the first nanometers of the InSb ZB base. Indeed
35 the relative intensity inversion observed (i.e., InAs shows As polarity, being In the heavier
36 constituent, red plot in Figure 1(c); while InSb presents Sb polarity being Sb the heavier, green
37 plot in Figure 1(c)) demonstrates that the interface between materials is not abrupt, as reported
38 previously for InAs/InSb nanowires⁶¹. Further strain analysis shown in Supporting Figure S4
39 along with EELS measurements confirm the alloying at the InAs/InSb interface over a few
40
41
42
43
44
45
46
47
48
49
50
51
52
53
54
55
56
57
58
59
60

1
2
3 nanometers. Focusing now on the InSb nanosail itself, all investigated samples were
4
5 characterized by a pristine ZB structure with the exception of a single longitudinal twin boundary
6
7 located at the base (see Figure 1(e)) and extending parallel to one of the {111} lateral facets of
8
9 the structures, disappearing at the corner (Figure 1(f)) where the new facet shrinking the
10
11 structure starts to develop. This single structural defect will be discussed in details in the
12
13 following and in Supporting Information..
14
15

16
17
18 Post-growth, the seed particles were found to be single AuIn₂ crystals with a cubic Fm3-m
19
20 structure (Figure 1 (g,h)), and perfectly lattice-matched to the nanosail: (-11-1) [110] AuIn₂ || (-
21
22 111)[110] InSb. The AuIn₂ composition is in agreement with the pseudo binary eutectic region
23
24 of the Au-In-Sb ternary phase diagram, as discussed in previous works^{35, 36, 62}. The interface
25
26 between the sail and the alloy metal particle is atomically flat, and there is no evidence of gold
27
28 diffusion within the nanosail structure. The particle exhibits low-index facets, as shown Figure
29
30 1(d), similar to those previously reported for InSb NWs⁶¹.
31
32
33
34
35
36
37
38
39
40
41
42
43
44
45
46
47
48
49
50
51
52
53
54
55
56
57
58
59
60

1
2
3 Having established that our nanostructures were of the highest crystalline quality we then
4
5 further investigate their faceting and 3D geometry using both experimental data and 3D atomistic
6
7 modelling. From the analysis of a combination of SEM images taken with both titled view and
8
9 plane view together with STEM images in different zone axes, a precise 3D atomistic model was
10
11 built. The final nanosail geometry was found to vary slightly depending on its development stage
12
13 (Figure 2 (a)-(d) and Supporting Figure S7) but all nanosails were characterized by several
14
15 common features, discussed below. Similarities among nanowires and nanosails cannot be
16
17 neglected and, indeed, as well as growing along the same direction, i.e., [-111], both
18
19 architectures shown a partial common faceting based on {110} planes. For the nanosails, the
20
21 frontal and back facets always correspond to {110} planes, i.e., (110) and (-1-10), as illustrated
22
23 in the [110] front view in Figure 2(e), but also the vertical side of the nanosail is composed by
24
25 two different {110} planes (i.e., (01-1) and (-10-1)). The bottom lateral side expanding outwards
26
27 and running parallel to the observed twin boundary, belongs to the (-11-1) plane, as well as the
28
29 upper parallel facet. It is noteworthy that the width of the twinned section is constant along its
30
31 length. The twin boundary is found to be an orthotwin^{63, 64} (see Supporting Figure S5) and more
32
33 details about its position and propagation are given in Supporting Figure S6. Two additional
34
35 {10 l } planes (usually {103}) complete the faceting of the whole morphology. In contrast to the
36
37 complex higher index facets present where the lateral twin terminates on the top left hand side of
38
39 the droplet, the {111} and {110} facets are all atomically flat. A root mean square roughness of
40
41 3.5Å has been extracted using atomic force microscopy (AFM).
42
43
44
45
46
47
48
49
50

51 In terms of the formation mechanism, a few observations should be made prior to describing a
52
53 growth scenario. First the nanosails retain two small {110} facets (extending directly from the
54
55 InAs “mast”) and two very large {110} facets of the original six {110} planes completing the
56
57
58
59
60

1
2
3 perfectly hexagonal shape of an InSb nanowire. Secondly, all nanosails possess the same pure
4 zinc blende crystal structure topped by a AuIn₂ alloy particle showing post-growth perfect strain-
5 free epitaxial relationship with the semiconductor, exactly as InSb nanowires do⁶¹. Finally the
6 growth conditions leading to the nanosail formation are obviously very close to those favorable
7 for the growth of InSb nanowires since they both grow simultaneously, sometimes within sub-
8 micron distances from each other, independently of the growth technique (MOVPE or MBE).
9 Therefore, the nanosail formation clearly shares very strong links to the metal-assisted nanowire
10 vapor liquid solid growth mechanism. In the same way, it was shown by several authors that
11 under certain conditions, III-V nanowires can kink to other crystallographic directions^{65, 66},
12 including to other polarities⁶⁷ or contain internal twins non-perpendicular to their elongation
13 axis^{68, 69}. In all the above examples it was either demonstrated or at least inferred that the alloyed
14 seed particle was allowed to unpin from its standard {111} growth plane to wet more than one
15 planes (multiple surfaces)⁷⁰, including the nanowire sidewalls. Even during standard growth of
16 diamond cubic or zinc blende nanowire crystals a corner oscillation has been confirmed by *in-*
17 *situ* growth inside TEMs⁷¹⁻⁷³.

18
19
20 Keeping in mind these considerations, Figure 2(f) illustrates our suggested phenomenological
21 growth scenario to account for the formation of the InSb nanosails. When switching from As to
22 Sb the droplet composition, phases and surface energy balance are changed dramatically. An
23 increase in diameter occurs immediately after the introduction of Sb in the alloyed In(As,Sb)
24 region a few nanometers above the InAs stem⁶¹. In agreement with a large set of published
25 experimental results^{39, 70}, the seed droplet is therefore allowed to unpin slightly from its position
26 lying on the (-111) InSb plane to wet the sidewalls. Such a configuration has been shown to
27 allow for new nucleation sites, and if two nuclei originating from two adjacent corners merge
28
29
30
31
32
33
34
35
36
37
38
39
40
41
42
43
44
45
46
47
48
49
50
51
52
53
54
55
56
57
58
59
60

1
2
3 together, a grain boundary/twin can easily form. Illustrations of the morphological and structural
4 signatures of this defect are shown in Supporting Figure S6. Once the inclined twin is formed the
5 droplet wets multiple facets: the usual (-111) facet and a new {110} facet or ensemble of
6
7 connected facets on its outer region (on the left, yellow pointed in Figure 2(f)). As the growth
8 proceeds along the directions indicated in blue, the droplet will be stretched until the limit of its
9 acceptable deformation in view of its surface tension. Such a dynamic modification of the
10 surface area under the droplet has been described and modelled in detail in the case of twinning
11 superlattices^{74, 75}, where a further conceptual similarity lies in growth occurring on planes not
12 perpendicular to the growth axis. After reaching its maximal surface tension the droplet will
13 eventually unpin from the inclined lateral facet(s) pointed in yellow in Figure 2(f), resulting in
14 the creation of the new facets that narrow the system. The situation shown in Figure 2(f) likely
15 occurs at a very early stage of the nanosails formation, where its lateral extent does not differ
16 much from that of a nanowire diameter. These sets of facets ({103} in the 3D model shown in
17 Figure 2(e)) will depend on growth kinetics and adapt accordingly. As growth proceeds under
18 the droplet, it may become more favorable for the droplet to stick to the {103}/(-111) triple
19 phase boundary instead at the edge formed by the {110}/(-111) planes depicted on the right hand
20 side in figure 2(f), leading to the creation of a new {-11-1} facet, exactly parallel to the bottom
21 left one. An animated movie on the formation of the nanosails, based on atomic 3D models, can
22 be found on-line⁷⁶. Now that all of the key facets have been formed, the miniature nanosail
23 grows *via* both vertical VLS and lateral Vapor Solid (VS) epitaxy to create the large surface area
24 nanosheets observed. Future *in-situ* TEM growth studies could refine our understanding of the
25 formation of such an original geometry⁷⁷.
26
27
28
29
30
31
32
33
34
35
36
37
38
39
40
41
42
43
44
45
46
47
48
49
50
51
52
53
54
55
56
57
58
59
60

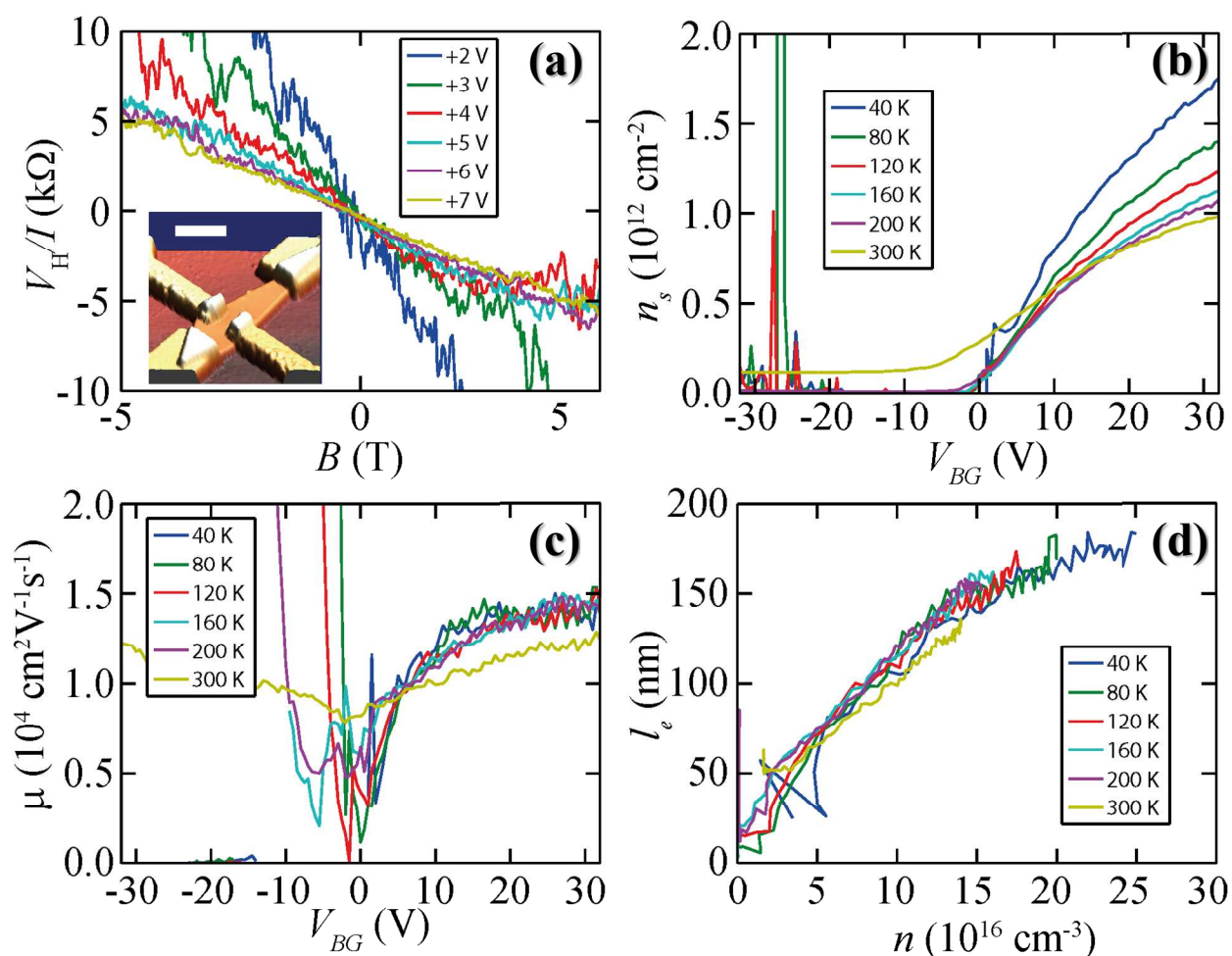


Figure 3: Hall measurements on InSb nanosails. (a) Hall voltage V_H as a function of the magnetic field applied perpendicular to the nanosail surface B for different voltages V_{BG} applied on the back-gate (values given in the legend) at a temperature of 2.1 K. Inset: AFM image of the four-terminal nanosail device (scale bar 500 nm). (b) Sheet electron density n_s as deduced from the Hall measurements using the single carrier model as a function of the back-gate voltage V_{BG}

1
2
3 and for different temperatures (values given in the legend). (c) Electron mobility μ as a function
4 of the back-gate voltage V_{BG} . The mobility is calculated from the sheet resistance measured in
5 the van der Pauw configuration and from the electron sheet density presented in panel (c). (d)
6 Elastic mean free path l_e as a function of the bulk carrier density n assuming a homogeneous
7 carrier distribution over the 70 nm thickness of the nanosail.
8
9

10
11
12
13
14
15
16 In order to assess the electronic quality of the InSb nanosails, we performed electrical
17 measurements in the van der Pauw geometry, as shown inset of Figure 3(a), using a highly
18 conductive n^+ Si substrate covered by 225 nm thermal SiO_2 oxide as a back gate to allow for
19 tuning of the carrier density. This geometry allows direct access to the carrier density through the
20 Hall effect, and to the intrinsic conductivity and carrier mobility through four-point
21 measurements. Figure 3(a) shows the Hall voltage measured as a function of the magnetic field
22 applied perpendicular to the nanosail surface. It follows the expected linear dependence with a
23 negative sign corresponding to electrons. In the following the Hall voltage has been measured at
24 +0.5 T and -0.5 T as a function of the gate voltage and temperature.
25
26
27
28
29
30
31
32
33
34
35
36
37

38 At high temperature, the dependence of the Hall voltage on the back gate voltage is non
39 monotonous, which is the signature of both electron and hole transport in a low band-gap
40 material (see Supporting Information Figure S8). At lower temperature and positive gate voltage,
41 only electrons participate in carrier transport, and we can therefore apply a single carrier model
42 to determine the sheet electron density n_s , which is plotted as a function of the back gate voltage
43 for different temperatures in Figure 3(b). At low temperature, the carrier density shows a
44 threshold and linear variation for a limited range of gate voltages. A fit of the linear region (gate
45 voltage range from +5 to +10 V) at 40 K gives a slope of $(1.36 \pm 0.13) \times 10^{-4} \text{ C.cm}^{-2}$ and a
46
47
48
49
50
51
52
53
54
55
56
57
58
59
60

1
2
3 threshold voltage of $V_T = 0.3 \pm 0.5$ V. The slope is close to the expected value of 1.5×10^{-4} C.cm⁻²
4
5
6 calculated from a plane capacitor model with the dielectric thickness of 225 nm.
7

8
9 We have measured the conductivity σ as a function of gate voltage and temperature using the
10 van der Pauw method⁷⁸ (see Supporting Information Section SF). Similar to the Hall voltage, the
11 conductivity at high temperature is a non-monotonous function of the gate voltage due to mixed
12 electron and hole transport. At positive gate voltage, however the conductivity is dominated by
13 electron transport due to the low mobility and density of holes. The electron mobility extracted in
14 the single-carrier model is plotted as a function of the gate voltage for different temperatures in
15 Figure 3(c). At room-temperature we find the mobility in our 70 nm-thick InSb nanosails to be
16 1.25×10^4 cm²V⁻¹.s⁻¹, a value less than that of bulk InSb (7.7×10^4 cm²V⁻¹.s⁻¹), but four times
17 larger than 70 nm-thick InSb layers grown on GaAs, and equal to that of 300 nm thick InSb
18 layers^{79, 80}. This improvement relative to the best values for an InSb layer of similar thickness
19 may be attributed to the absence of strain and dislocations that are inherent to the growth on
20 substrate with large lattice mismatch, and demonstrates the significant potential of the nanosail
21 geometry in realizing planar devices.
22
23
24
25
26
27
28
29
30
31
32
33
34
35
36
37
38
39

40 The mobility is weakly dependent on temperature (see Supporting Information SF.3), and is
41 therefore most probably limited by defect scattering. Due to the absence of structural defects in
42 the nanosail (apart from the single twin as discussed above), we attribute the origin of the
43 scattering to defects close to the InSb surface, either traps in the SiO₂ dielectrics, at the
44 SiO₂/InSb interface or the top surface²². We have also deduced the electron mean free path $l_e =$
45 $v_F \tau_e$ from the average scattering time $\tau_e = m^* \mu / e$, and the 3D Fermi velocity $v_F = \hbar k_F / m^* =$
46 $(\hbar / m^*) (3\pi^2 n)^{1/3}$, where n is the electron density. l_e is plotted as a function of n for different
47 temperatures in Figure 3(d). That the mobility shows a weak temperature dependence suggests a
48
49
50
51
52
53
54
55
56
57
58
59
60

1
2
3 scattering mechanism other than phonon scattering dominates. Previous work has shown
4
5 passivation to improve the mobility and mean-free path of nanostructures⁸¹⁻⁸³. The relatively
6
7 large values of l_e found here holds realistic promise for the realization of ballistic transport in
8
9 future nanosail devices.
10
11

12
13 In order to test the possibility of realizing ballistic quantum devices from our InSb nanosails,
14
15 we have fabricated a constriction on a nanosail by depositing two top gates as shown in the inset
16
17 of Figure 4(a). Such a constriction, also known as quantum point contact^{55,56}, is expected to lead
18
19 to quasi-1D electronic transport. We emphasize here that such quasi-1D transport was expected
20
21 in InSb nanowires, but was only demonstrated at high magnetic field because back-scattering at
22
23 the contacts leads to a destruction of the signatures of 1D transport⁵⁷. Up until now 1D transport
24
25 in InSb was only demonstrated in 2D electron gases formed in InSb heterostructures⁸⁴, or in InSb
26
27 nanowires in the presence of an in-plane magnetic field⁵⁷.
28
29
30
31
32

33
34 The device with top gates showed a strong increase in resistance compared to devices without
35
36 top gates at zero applied top-gate voltage, which is presumably due to a depletion of the nanosail
37
38 below the top gates. We further observed that the resistance did not significantly vary with
39
40 application of top-gate voltage, giving further indication of this total depletion.
41
42
43

44
45 The conductance of a quasi-1D constriction is expected to be tuned either by changing the
46
47 width W of the constriction, or by changing the electron wave vector by changing the electron
48
49 density. In the following we have chosen to tune the carrier density in the constriction by using
50
51 the back gate instead of tuning the width of the constriction by using the top gate voltage due to
52
53 instabilities appearing when tuning the top gate, probably due to traps in the dielectric layer.
54
55
56
57
58
59
60

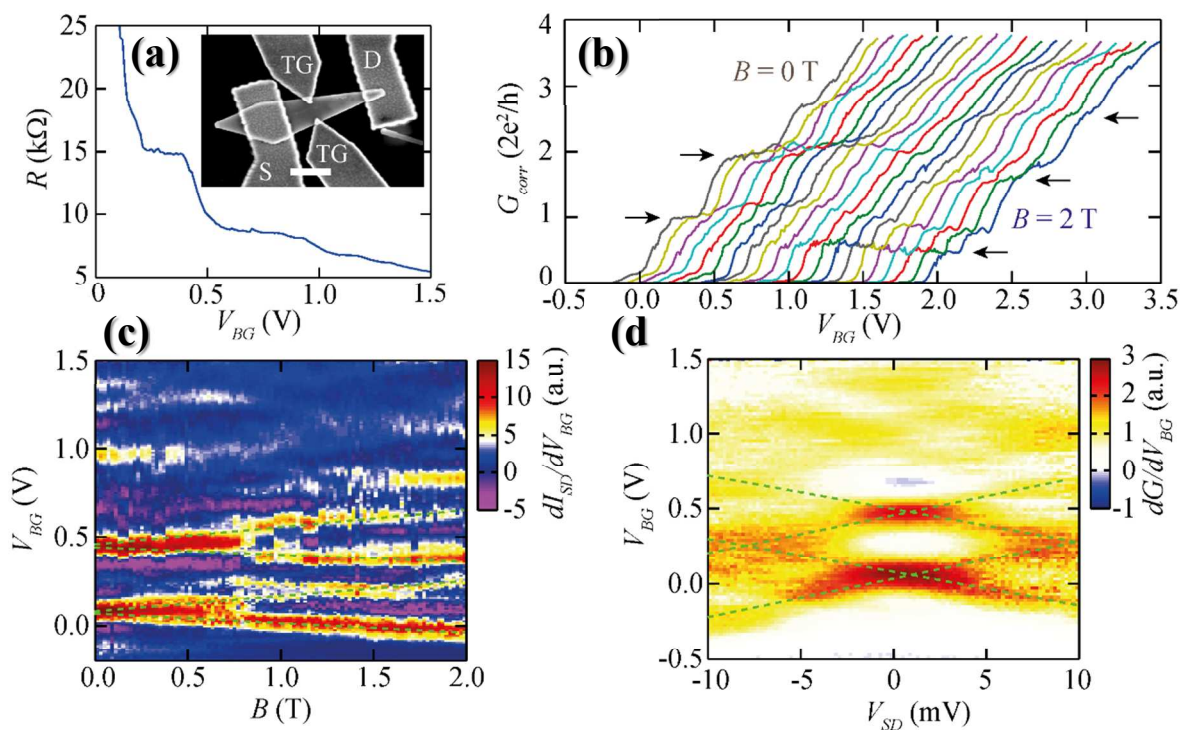


Figure 4. Top-gated quantum point contact to an InSb nanosail. (a) Two-point source-drain resistance of the device as a function of the back-gate voltage V_{BG} for a fixed voltage applied to the top-gates $V_{TG} = +0.68$ V and measured at $T = 6$ K. Inset: image of the top-gated quantum point contact device showing source and drain contacts, and two top gates electrically isolated from the nanosail by 10 nm of HfO_2 deposited by atomic layer deposition. (b) Corrected conductance of the device obtained after removing a 2 k Ω series resistance from the two-terminal resistance, corresponding to the contact resistance (see main text), as a function of the back-gate voltage and varying the parallel magnetic field in steps of 0.1 T from 0 to 2 T. The measurement has been performed at $T = 6$ K, and the curves have been laterally shifted by 0.1 V for clarity. The arrows emphasize the steps corresponding to conductance quantization. (c) Color map of $G = dI_{SD}/dV_{BG}$ as a function of the parallel magnetic field and the back-gate voltage emphasizing the conductance steps. The green dashed lines show the splitting of the two first conductance steps measured at $T = 2.1$ K. (d) Color-map of dG/dV_{BG} as a function of the source-

1
2
3 drain bias voltage V_{SD} and the back-gate voltage V_{BG} for $V_{TG} = +0.68$ V and $T = 6$ K. The green
4
5 dashed lines show the edge of the conduction steps.
6
7

8
9 The two-terminal resistance of the top-gated device is shown as a function of the back-gate
10 voltage for a fixed top-gate voltage $V_{tg} = +0.68$ V in Figure 4(a). This curve, obtained at zero
11 magnetic field, clearly shows two plateaux at about 15 k Ω (instead of $h/2e^2 = 12.9$ k Ω) and 8.5
12 k Ω (instead of $h/4e^2 = 6.5$ k Ω) respectively. For quasi-1D electronic transport at zero magnetic
13 field such plateaux are expected as $h/2e^2 = 12.9$ k Ω and $h/4e^2 = 6.5$ k Ω . We attribute the constant
14 difference to a contact series resistance of about 2 k Ω , as well as the resistance of the nanosail
15 outside the constriction. This resistance is compatible with the two-terminal resistance obtained
16 in a device with no top gate (such as the one investigated in Figure 3). In order to emphasize
17 further the quantification of the conductance in units of $2e^2/h$, as expected for a quantum point
18 contact, we have plotted the two-terminal conductance corrected by the series resistance of 2 k Ω
19 in Figure 4(b). Here a magnetic field parallel to the plane of the nanosail is applied in order to
20 split the 1D subbands. We see in this plot that the two plateaux at $2e^2/h$ and $4e^2/h$ disappear at a
21 magnetic field of 2 T and give rise to plateaux at e^2/h , $3e^2/h$ and $5e^2/h$. Such behaviour can be
22 explain by the splitting of the 1D sub-bands as a function of the magnetic field, and further
23 confirms that the plateaux are related to 1D transport.
24
25
26
27
28
29
30
31
32
33
34
35
36
37
38
39
40
41
42
43
44

45 We also investigated the splitting of the 1D sub-bands quantitatively as a function of applied
46 magnetic field. In Figure 4(c) we plot the differential conductance $G = dI_{SD}/dV_{BG}$ in order to
47 emphasize the edges of the plateaux. In this plot we clearly observe the splitting of the two first
48 sub-bands. This splitting should occur at a rate of $g^* \mu_B B$. In our case the splitting is 0.146 V/T for
49 both sub-bands. In order to determine the lever arm of the back-gate (the change in Fermi energy
50 as a function of the back-gate voltage), we have measured the non-linear conductance, i.e. the
51
52
53
54
55
56
57
58
59
60

1
2
3 change in the conductance as a function of the source-drain bias voltage. We see in Figure 4(d)
4 that the edges of the plateaux split at finite source-drain bias voltage with a rate corresponding to
5 a lever arm of 19.6 meV/V. We then determine a magnetic field splitting of 2.86 meV/T, and a
6 Landé g-factor $|g^*| = 49$, which is close to the expected bulk value of 51.
7
8
9

10
11
12
13
14 Finally, we investigated the effect of the top-gate voltage on the level spacing. From non-linear
15 conductance measurements, we have determined the level spacing between the first two sub-
16 bands at zero magnetic field (Supporting Information section SF.4). The energy for a top-gate
17 voltage $V_{TG} = +0.68$ V is $E_2 - E_1 = 8.7$ meV, corresponding to a constriction of width 80 nm (for
18 an infinite 1D square potential, with an electron effective mass $m^* = m_0$). The level spacing for
19 $V_{TG} = -1$ V is $E_2 - E_1 = 11.1$ meV, corresponding to a constriction of width 70 nm. This
20 dependence further confirms that the quasi-1D channel is formed in-between the two top-gates.
21
22
23
24
25
26
27
28
29
30

31
32 In conclusion we synthesized free-standing, high performance InSb nanostructures with a
33 sheet-like morphology. This novel morphology is characterized by large atomically flat {110}
34 surfaces and results from a single lateral twinning event. We measure a high electron mobility
35 which is promising for both low power nanoelectronics and low temperature transport physics.
36 Demonstration of quantized conductance in a quantum point contact at zero in-plane magnetic
37 field further attests to material quality and the potential for spin-orbit quantum physics
38 applications. We expect that the outlined growth mechanism may be generalized to other
39 materials grown by VLS delivering a readily contacted 2D-like geometry for complex radial
40 heterostructures and topological quantum physics experiments⁸⁵. Future work on more advanced
41 device geometries such as suspended nanomembrane devices^{86, 87} or using dielectric/chemical
42 passivation schemes^{81-83, 88} could enhance their promising transport figures of merit even further.
43
44
45
46
47
48
49
50
51
52
53
54
55
56
57
58
59
60

ASSOCIATED CONTENT

Supporting Information. Methods, Growth, Characterization and Device Processing, SA. Statistics on the yield of different morphologies, SB (Figures S1-S3). Analysis of the InAs/InSb interface, SC (Figure S4). Presence of a unique twin boundary, SD (Figures S5, S6). Faceting of the nanosails, SE (Figure S7). Electrical measurements, SF (Figures S8-S11) This material is available free of charge via the Internet at <http://pubs.acs.org>.

AUTHOR INFORMATION

Corresponding Authors

*Emails: philippe.caroff@anu.edu.au, renaud.leturcq@list.lu, arbiol@icrea.cat

Present Address:

†SPEC, CEA, CNRS, Université Paris-Saclay, CEA Saclay 91191 Gif-sur-Yvette, France

Author Contributions

P.C. and R. L. conceived the idea for the research, co-lead the project and performed respectively the material growth/morphological analyses and most of the device processing/measurements.

M. M. performed the complete atomic resolution transmission electron microscopy analysis and built the 3D model as a result of the analysis, under the supervision of and with inputs from J.A., C. M., S.R.P., and P. C., whom altogether discussed and analyzed the growth and structural information. C. R. was involved in the device processing and measurements under the

1
2
3 supervision of R. L.. All authors commented on the work and provided valuable input throughout
4
5 the project. P. C. wrote the manuscript with significant contributions from all authors.
6
7

8 9 **Funding Sources**

10
11 This research was supported in part by the French ANR through the TERADOT Project No.
12
13 ANR-11-JS04-002-01, the Ministry of Higher Education and Research, Nord-Pas de Calais and
14
15 Mid-Pyrénées Regional Council and FEDER through the “Contrat de Projets Etat Region
16
17 (CPER) 2007-2013”, IDEX WirOnSi, the Australian Research Council, through the Future
18
19 Fellowship program, grant number FT120100498, the Generalitat de Catalunya 2014 SGR 1638,
20
21 and the Spanish MINECO MAT2014-51480-ERC (e-ATOM).
22
23
24

25 26 **Notes**

27
28 The authors declare no competing financial interests.
29
30
31
32

33 34 **ACKNOWLEDGMENT**

35
36 P.C., and R. L. thank Xavier Wallart for scientific discussions related to MBE growth,
37
38 Christophe Coinon and Jean-Louis Codron for technical support on the MBE, and Christophe
39
40 Boyaval for support on SEM imaging. P.C., S.R.P and J. A. thank Dr Jerry Tersoff for fruitful
41
42 discussions regarding the nanosail growth mechanisms. Tim burgess is acknowledged for
43
44 scientific discussions and for proof-reading the manuscript. The MBE growth has been
45
46 conducted in, and supported by, the EIPHY group lead by Xavier Wallart at IEMN. The
47
48 microscopy works have been conducted in the "Laboratorio de Microscopias Avanzadas" at
49
50 "Instituto de Nanociencia de Aragon - Universidad de Zaragoza". J.A. and M.d.l.M. thank the
51
52 LMA-INA for offering access to their instruments and expertise.
53
54
55
56
57
58
59
60

REFERENCES

1. Yan, R.; Gargas, D.; Yang, P. *Nat. Photonics* **2009**, 3, (10), 569-576.
2. Vitiello, M. S.; Viti, L.; Coquillat, D.; Knap, W.; Ercolani, D.; Sorba, L. *APL Mater.* **2015**, 3, (2), 026104.
3. Riel, H.; Wernersson, L.-E.; Hong, M.; del Alamo, J. A. *MRS Bull.* **2014**, 39, (08), 668-677.
4. Wernersson, L.-E. *J. Appl. Phys.* **2015**, 117, (11), 112810.
5. Frolov, S. M.; Plissard, S. R.; Nadj-Perge, S.; Kouwenhoven, L. P.; Bakkers, E. P. A. M. *MRS Bull.* **2013**, 38, (10), 809-815.
6. Tomioka, K.; Fukui, T. *Nano Lett.* **2015**, 15, (11), 7189.
7. Svensson, J.; Dey, A. W.; Jacobsson, D.; Wernersson, L.-E. *Nano Lett.* **2015**.
8. Tomioka, K.; Yoshimura, M.; Fukui, T. *Nature* **2012**, 488, (7410), 189-192.
9. Lind, E.; Memisevic, E.; Dey, A. W.; Wernersson, L. E. *IEEE J. Electron Devices Soc.* **2015**, 3, (3), 96-102.
10. Yan, C.; Li, X.; Zhou, K.; Pan, A.; Werner, P.; Mensah, S. L.; Vogel, A. T.; Schmidt, V. *Nano Lett.* **2012**, 12, (4), 1799-1805.
11. Svensson, J.; Anttu, N.; Vainorius, N.; Borg, B. M.; Wernersson, L.-E. *Nano Lett.* **2013**, 13, (4), 1380-1385.
12. Duan, X.; Huang, Y.; Agarwal, R.; Lieber, C. M. *Nature* **2003**, 421, (6920), 241-245.
13. Qian, F.; Li, Y.; Gradecak, S.; Park, H.-G.; Dong, Y.; Ding, Y.; Wang, Z. L.; Lieber, C. M. *Nat. Mater.* **2008**, 7, (9), 701-706.
14. Chen, R.; Tran, T.-T. D.; Ng, K. W.; Ko, W. S.; Chuang, L. C.; Sedgwick, F. G.; Chang-Hasnain, C. *Nat. Photonics* **2011**, 5, (3), 170-175.

- 1
2
3
4
5
6
7
8
9
10
11
12
13
14
15
16
17
18
19
20
21
22
23
24
25
26
27
28
29
30
31
32
33
34
35
36
37
38
39
40
41
42
43
44
45
46
47
48
49
50
51
52
53
54
55
56
57
58
59
60
15. Hicks, L. D.; Dresselhaus, M. S. *Phys. Rev. B* **1993**, 47, (24), 16631-16634.
 16. Boukai, A. I.; Bunimovich, Y.; Tahir-Kheli, J.; Yu, J.-K.; Goddard Iii, W. A.; Heath, J. R. *Nature* **2008**, 451, (7175), 168-171.
 17. Yamaguchi, S.; Matsumoto, T.; Yamazaki, J.; Kaiwa, N.; Yamamoto, A. *Appl. Phys. Lett.* **2005**, 87, (20), 201902.
 18. Mingo, N. *Appl. Phys. Lett.* **2004**, 84, (14), 2652-2654.
 19. Uryupin, O. N.; Vedernikov, M. V.; Shabaldin, A. A.; Ivanov, Y. V.; Kumzerov, Y. A.; Fokin, A. V. *J. Electron. Mater.* **2009**, 38, (7), 990-993.
 20. Mensch, P.; Karg, S.; Schmidt, V.; Gotsmann, B.; Schmid, H.; Riel, H. *Appl. Phys. Lett.* **2015**, 106, (9), 093101.
 21. Nilsson, H. A.; Caroff, P.; Thelander, C.; Larsson, M.; Wagner, J. B.; Wernersson, L.-E.; Samuelson, L.; Xu, H. Q. *Nano Lett.* **2009**, 9, (9), 3151-3156.
 22. Gül, Ö.; J. van Woerkom, D.; Weperen, I. v.; Car, D.; Plissard, S. R.; Bakkers, E., P. A. M.; Kouwenhoven, L., P. *Nanotechnol.* **2015**, 26, (21), 215202.
 23. Nilsson, H. A.; Karlström, O.; Larsson, M.; Caroff, P.; Pedersen, J. N.; Samuelson, L.; Wacker, A.; Wernersson, L. E.; Xu, H. Q. *Phys. Rev. Lett.* **2010**, 104, (18), 186804.
 24. Pribiag, V. S.; Nadj Perge, S.; Frolov, S. M.; van den Berg, J. W. G.; van Weperen, I.; Plissard, S. R.; Bakkers, E. P. A. M.; Kouwenhoven, L. P. *Nat. Nanotechnol.* **2013**, 8, (3), 170-174.
 25. Nadj-Perge, S.; Pribiag, V. S.; van den Berg, J. W. G.; Zuo, K.; Plissard, S. R.; Bakkers, E. P. A. M.; Frolov, S. M.; Kouwenhoven, L. P. *Phys. Rev. Lett.* **2012**, 108, (16), 166801.
 26. van den Berg, J. W. G.; Nadj-Perge, S.; Pribiag, V. S.; Plissard, S. R.; Bakkers, E. P. A. M.; Frolov, S. M.; Kouwenhoven, L. P. *Phys. Rev. Lett.* **2013**, 110, (6), 066806.

- 1
2
3 27. Mourik, V.; Zuo, K.; Frolov, S. M.; Plissard, S. R.; Bakkers, E. P. A. M.; Kouwenhoven,
4 L. P. *Science* **2012**, 336, (6084), 1003-1007.
5
6
7
8 28. Deng, M. T.; Yu, C. L.; Huang, G. Y.; Larsson, M.; Caroff, P.; Xu, H. Q. *Nano Lett.*
9
10 **2012**, 12, (12), 6414-6419.
11
12 29. Deng, M. T.; Yu, C. L.; Huang, G. Y.; Larsson, M.; Caroff, P.; Xu, H. Q. *Sci. Rep.* **2014**,
13 4, 7261.
14
15
16
17 30. Borg, B. M.; Wernersson, L.-E. *Nanotechnol.* **2013**, 24, (20), 202001.
18
19 31. Caroff, P.; Messing, M., E.; Borg, B. M.; Dick, K., A. ; Deppert, K.; Wernersson, L.-E.
20
21 *Nanotechnol.* **2009**, 20, (49), 495606.
22
23 32. Li, A.; Sibirev, N. V.; Ercolani, D.; Dubrovskii, V. G.; Sorba, L. *Cryst. Growth Des.*
24
25 **2013**, 13, (2), 878-882.
26
27
28 33. Plissard, S. R.; Slapak, D. R.; Verheijen, M. A.; Hocevar, M.; Immink, G. W. G.; van
29 Weperen, I.; Nadj-Perge, S.; Frolov, S. M.; Kouwenhoven, L. P.; Bakkers, E. P. A. M. *Nano*
30
31 *Lett.* **2012**, 12, (4), 1794-1798.
32
33 34. Park, H. D.; Prokes, S. M.; Twigg, M. E.; Ding, Y.; Wang, Z. L. *J. Cryst. Growth*
34
35 **2007**, 304, (2), 399-401.
36
37 35. Caroff, P.; Wagner, J. B.; Dick, K. A.; Nilsson, H. A.; Jeppsson, M.; Deppert, K.;
38 Samuelson, L.; Wallenberg, L. R.; Wernersson, L.-E. *Small* **2008**, 4, (7), 878-882.
39
40 36. Ercolani, D.; Rossi, F.; Li, A.; Roddaro, S.; Grillo, V.; Salviati, G.; Beltram, F.; Sorba, L.
41
42 *Nanotechnol.* **2009**, 20, (50), 505605.
43
44
45 37. Thelander, C.; Caroff, P.; Plissard, S.; Dick, K. A. *Appl. Phys. Lett.* **2012**, 100, (23),
46
47 232105.
48
49
50
51
52
53
54
55
56
57
58
59
60

- 1
2
3
4
5
6
7
8
9
10
11
12
13
14
15
16
17
18
19
20
21
22
23
24
25
26
27
28
29
30
31
32
33
34
35
36
37
38
39
40
41
42
43
44
45
46
47
48
49
50
51
52
53
54
55
56
57
58
59
60
38. Gorji Ghalamestani, S.; Ek, M.; Ganjipour, B.; Thelander, C.; Johansson, J.; Caroff, P.; Dick, K. A. *Nano Lett.* **2012**, 12, (9), 4914-4919.
39. Plissard, S. R.; van Weperen, I.; Car, D.; Verheijen, M. A.; Immink, G. W. G.; Kammhuber, J.; Cornelissen, L. J.; Szombati, D. B.; Geresdi, A.; Frolov, S. M.; Kouwenhoven, L. P.; Bakkers, E. P. A. M. *Nat. Nanotechnol.* **2013**, 8, (11), 859-864.
40. Car, D.; Wang, J.; Verheijen, M. A.; Bakkers, E. P. A. M.; Plissard, S. R. *Adv. Mater.* **2014**, 26, (28), 4875-4879.
41. Uccelli, E.; Arbiol, J.; Magen, C.; Krogstrup, P.; Russo-Averchi, E.; Heiss, M.; Mugny, G.; Morier-Genoud, F.; Nygård, J.; Morante, J. R.; Fontcuberta i Morral, A. *Nano Lett.* **2011**, 11, (9), 3827-3832.
42. Utama, M. I. B.; de la Mata, M.; Magen, C.; Arbiol, J.; Xiong, Q. *Adv. Funct. Mater.* **2013**, 23, (13), 1636-1646.
43. Dayeh, S. A.; Wang, J.; Li, N.; Huang, J. Y.; Gin, A. V.; Picraux, S. T. *Nano Lett.* **2011**, 11, (10), 4200-4206.
44. Blömers, C.; Grap, T.; Lepsa, M. I.; Moers, J.; Trelenkamp, S.; Grützmacher, D.; Lüth, H.; Schäpers, T. *Appl. Phys. Lett.* **2012**, 101, (15), 152106.
45. Storm, K.; Halvardsson, F.; Heurlin, M.; Lindgren, D.; Gustafsson, A.; Wu, P. M.; Monemar, B.; Samuelson, L. *Nat. Nanotechnol.* **2012**, 7, (11), 718-722.
46. Schelter, J.; Bohr, D.; Trauzettel, B. *Phys. Rev. B* **2010**, 81, (19), 195441.
47. Nikoobakht, B.; Li, X. *ACS Nano* **2012**, 6, (3), 1883-1887.
48. Arab, S.; Chi, C.-Y.; Shi, T.; Wang, Y.; Dapkus, D. P.; Jackson, H. E.; Smith, L. M.; Cronin, S. B. *ACS Nano* **2015**, 9, (2), 1336-1340.

- 1
2
3
4 49. Chang, C.-C.; Chi, C.-Y.; Chen, C.-C.; Huang, N.; Arab, S.; Qiu, J.; Povinelli, M.;
5
6 Dapkus, P. D.; Cronin, S. *Nano Res.* **2014**, 7, (2), 163-170.
7
8 50. Aagesen, M.; Johnson, E.; Sorensen, C. B.; Mariager, S. O.; Feidenhans'l, R.; Spiecker,
9
10 E.; Nygard, J.; Lindelof, P. E. *Nat. Nanotechnol.* **2007**, 2, (12), 761-764.
11
12 51. Conesa-Boj, S.; Russo-Averchi, E.; Dalmau-Mallorqui, A.; Trevino, J.; Pecora, E. F.;
13
14 Forestiere, C.; Handin, A.; Ek, M.; Zweifel, L.; Wallenberg, L. R.; Ruffer, D.; Heiss, M.;
15
16 Troadec, D.; Dal Negro, L.; Caroff, P.; Fontcuberta i Morral, A. *ACS Nano* **2012**, 6, (12), 10982-
17
18 10991.
19
20 52. Hsu, C.-W.; Chen, Y.-F.; Su, Y.-K. *Nanoscale Res. Lett.* **2012**, 7, (1), 642.
21
22 53. Chi, C.-Y.; Chang, C.-C.; Hu, S.; Yeh, T.-W.; Cronin, S. B.; Dapkus, P. D. *Nano Lett.*
23
24 **2013**, 13, (6), 2506-2515.
25
26 54. Tutuncuoglu, G.; de la Mata, M.; Deiana, D.; Potts, H.; Matteini, F.; Arbiol, J.;
27
28 Fontcuberta i Morral, A. *Nanoscale* **2015**, 7, (46), 19453-19460.
29
30 55. Wharam, D. A.; Thornton, T. J.; Newbury, R.; Pepper, M.; Ahmed, H.; Frost, J. E. F.;
31
32 Hasko, D. G.; Peacock, D. C.; Ritchie, D. A.; Jones, G. A. C. *J. Phys. C: Solid State Phys.* **1988**,
33
34 21, (8), L209.
35
36 56. van Wees, B. J.; van Houten, H.; Beenakker, C. W. J.; Williamson, J. G.; Kouwenhoven,
37
38 L. P.; van der Marel, D.; Foxon, C. T. *Phys. Rev. Lett.* **1988**, 60, (9), 848-850.
39
40 57. van Weperen, I.; Plissard, S. R.; Bakkers, E. P. A. M.; Frolov, S. M.; Kouwenhoven, L.
41
42 *P. Nano Lett.* **2013**, 13, (2), 387-391.
43
44 58. Bernal, S.; Botana, F. J.; Calvino, J. J.; López-Cartes, C.; Pérez-Omil, J. A.; Rodríguez-
45
46 Izquierdo, J. M. *Ultramicroscopy* **1998**, 72, (3-4), 135-164.
47
48
49
50
51
52
53
54
55
56
57
58
59
60

- 1
2
3
4
5
6
7
8
9
10
11
12
13
14
15
16
17
18
19
20
21
22
23
24
25
26
27
28
29
30
31
32
33
34
35
36
37
38
39
40
41
42
43
44
45
46
47
48
49
50
51
52
53
54
55
56
57
58
59
60
59. Arbiol, J.; Cirera, A.; Peiró, F.; Cornet, A.; Morante, J. R.; Delgado, J. J.; Calvino, J. J. *Appl. Phys. Lett.* **2002**, 80, (2), 329-331.
60. de la Mata, M.; Magen, C.; Gazquez, J.; Utama, M. I. B.; Heiss, M.; Lopatin, S.; Furtmayr, F.; Fernández-Rojas, C. J.; Peng, B.; Morante, J. R.; Rurali, R.; Eickhoff, M.; Fontcuberta i Morral, A.; Xiong, Q.; Arbiol, J. *Nano Lett.* **2012**, 12, (5), 2579-2586.
61. de la Mata, M.; Magén, C.; Caroff, P.; Arbiol, J. *Nano Lett.* **2014**, 14, (11), 6614-6620.
62. Philipose, U.; Gopal, S.; Salfi, J.; Harry, E. R. *Semicond. Sci. Technol.* **2010**, 25, (7), 075004.
63. Cohen, D.; McKernan, S.; Carter, C. B. *Microsc. Microanal.* **1999**, 5, (03), 173-186.
64. Holt, D. B. *J Mater Sci* **1984**, 19, (2), 439-446.
65. Wang, J.; Plissard, S. R.; Verheijen, M. A.; Feiner, L.-F.; Cavalli, A.; Bakkers, E. P. A. *M. Nano Lett.* **2013**, 13, (8), 3802-3806.
66. Fonseka, H. A.; Caroff, P.; Wong-Leung, J.; Ameruddin, A. S.; Tan, H. H.; Jagadish, C. *ACS Nano* **2014**, 8, (7), 6945-6954.
67. Yuan, X.; Caroff, P.; Wong-Leung, J.; Fu, L.; Tan, H. H.; Jagadish, C. *Adv. Mater.* **2015**, 27, (40), 6096-6103.
68. Oliveira, D. S.; Tizei, L. H. G.; Li, A.; Vasconcelos, T. L.; Senna, C. A.; Archanjo, B. S.; Ugarte, D.; Cotta, M. A. *Nanoscale* **2015**, 7, (29), 12722-12727.
69. Yuan, X.; Caroff, P.; Wong-Leung, J.; Tan, H. H.; Jagadish, C. *Nanoscale* **2015**, 7, (11), 4995-5003.
70. Hocevar, M.; Immink, G.; Verheijen, M.; Akopian, N.; Zwiller, V.; Kouwenhoven, L.; Bakkers, E. *Nat. Commun.* **2012**, 3, 1266.

- 1
2
3
4
5
6
7
8
9
10
11
12
13
14
15
16
17
18
19
20
21
22
23
24
25
26
27
28
29
30
31
32
33
34
35
36
37
38
39
40
41
42
43
44
45
46
47
48
49
50
51
52
53
54
55
56
57
58
59
60
71. Oh, S. H.; Chisholm, M. F.; Kauffmann, Y.; Kaplan, W. D.; Luo, W.; Rühle, M.; Scheu, C. *Science* **2010**, 330, (6003), 489-493.
72. Gamalski, A. D.; Ducati, C.; Hofmann, S. *J. Phys. Chem. C* **2011**, 115, (11), 4413-4417.
73. Wen, C. Y.; Tersoff, J.; Hillerich, K.; Reuter, M. C.; Park, J. H.; Kodambaka, S.; Stach, E. A.; Ross, F. M. *Phys. Rev. Lett.* **2011**, 107, (2), 025503.
74. Algra, R. E.; Verheijen, M. A.; Borgstrom, M. T.; Feiner, L.-F.; Immink, G.; van Enckevort, W. J. P.; Vlieg, E.; Bakkers, E. P. A. M. *Nature* **2008**, 456, (7220), 369-372.
75. Burgess, T.; Breuer, S.; Caroff, P.; Wong-Leung, J.; Gao, Q.; Hoe Tan, H.; Jagadish, C. *ACS Nano* **2013**, 7, (9), 8105-8114.
76. <http://www.gaen.cat/research/279>.
77. Gamalski, A. D.; Voorhees, P. W.; Ducati, C.; Sharma, R.; Hofmann, S. *Nano Lett.* **2014**, 14, (3), 1288-1292.
78. Pauw, L. J. v. d. *Philips Tech. Rev.* **1958**, 13, 220.
79. Zhang, T.; Clowes, S. K.; Debnath, M.; Bennett, A.; Roberts, C.; Harris, J. J.; Stradling, R. A.; Cohen, L. F.; Lyford, T.; Fewster, P. F. *Appl. Phys. Lett.* **2004**, 84, (22), 4463-4465.
80. Zhang, T.; Harris, J. J.; Branford, W. R.; Bugoslavsky, Y. V.; Clowes, S. K.; Cohen, L. F.; Husmann, A.; Solin, S. A. *Appl. Phys. Lett.* **2006**, 88, (1), 012110.
81. Ko, H.; Takei, K.; Kapadia, R.; Chuang, S.; Fang, H.; Leu, P. W.; Ganapathi, K.; Plis, E.; Kim, H. S.; Chen, S.-Y.; Madsen, M.; Ford, A. C.; Chueh, Y.-L.; Krishna, S.; Salahuddin, S.; Javey, A. *Nature* **2010**, 468, (7321), 286-289.
82. Ford, A. C.; Kumar, S. B.; Kapadia, R.; Guo, J.; Javey, A. *Nano Lett.* **2012**, 12, (3), 1340-1343.

- 1
2
3
4
5
6
7
8
9
10
11
12
13
14
15
16
17
18
19
20
21
22
23
24
25
26
27
28
29
30
31
32
33
34
35
36
37
38
39
40
41
42
43
44
45
46
47
48
49
50
51
52
53
54
55
56
57
58
59
60
83. Potts, H.; Friedl, M.; Amaduzzi, F.; Tang, K.; Tütüncüoğlu, G.; Matteini, F.; Alarcon Lladó, E.; McIntyre, P. C.; Fontcuberta i Morral, A. *Nano Lett.* **2015**.
84. Goel, N.; Graham, J.; Keay, J. C.; Suzuki, K.; Miyashita, S.; Santos, M. B.; Hirayama, Y. *Physica E* **2005**, 26, (1-4), 455-459.
85. Gluschke, J. G.; Leijnse, M.; Ganjipour, B.; Dick, K. A.; Linke, H.; Thelander, C. *ACS Nano* **2015**, 9, (7), 7033-7040.
86. Bolotin, K. I.; Sikes, K. J.; Jiang, Z.; Klima, M.; Fudenberg, G.; Hone, J.; Kim, P.; Stormer, H. L. *Solid State Commun.* **2008**, 146, (9–10), 351-355.
87. Schmidt, M.; Schneider, G.; Heyn, C.; Stemmann, A.; Hansen, W. J. *Electron. Mater.* **2012**, 41, (6), 1286-1289.
88. Suyatin, D. B.; Thelander, C.; Björk, M. T.; Maximov, I.; Samuelson, L. *Nanotechnology* **2007**, 18, (10), 105307.

FOR TOC ONLY

